A RELAXED WISHART MODEL FOR POLARIMETRIC SAR DATA

Stian Normann Anfinsen, Torbjørn Eltoft, and Anthony Paul Doulgeris

University of Tromsø, Department of Physics and Technology, NO-9037 Tromsø, Norway,
E-mail: {stian.normann.anfinsen, torbjorn.eltoft, anthony.p.doulgeris}@uit.no

ABSTRACT

In this paper we demonstrate that simple yet flexible modelling of multilook polarimetric synthetic aperture radar (PolSAR) data can be obtained through a relaxation of the Wishart model. The degrees of freedom of the complex Wishart distribution is treated as a spatially nonstationary parameter, which is allowed to vary between thematic classes and segments of the PolSAR scene.

Key words: synthetic aperture radar; polarimetry; statistical modelling; Wishart distribution.

1. INTRODUCTION

The Wishart distribution is the de facto statistical model for multilook PolSAR data. It is based on the assumption that the complex scattering coefficients are jointly circular Gaussian. However, this is only satisfied for homogeneous areas with fully developed speckle and no texture, which renders the model inadequate in many cases. Improved modelling is achieved by using more complex models that account for texture, such as the polarimetric $\mathcal{G}$ distribution family [1], with the polarimetric $\mathcal{K}$ distribution [2] as a special case. These models allow for better adaption to data whose distribution is heavy-tailed and non-Gaussian, but this comes at the cost of higher mathematical complexity.

The comparatively higher mathematical tractability of the Wishart distribution motivates us to pursue a relaxed Wishart model as an alternative. In the context of multilook PolSAR data, the degrees of freedom of the Wishart distribution is interpreted as the equivalent number of looks, a constant, global value that quantifies the effective number of data samples averaged in the multilooking process. In contrast, we treat it as a free parameter, which varies between, and possibly also within, classes and segments of the PolSAR scene. This reflects the highly variable degree of smoothing imposed on the data by nonlinear speckle filters. The choice can also be justified by looking at the degrees of freedom as a shape parameter of the distribution, which is determined not only by the degree of averaging, but also by texture. Thus, the influence of multilooking, speckle filtering, and texture is assimilated into one parameter, which can be estimated efficiently with a recently proposed estimator [3, 4]

Sec. 2 reviews some existing density models for multilook PolSAR data and proposes the relaxed Wishart distribution as an alternative. In Sec. 3 we derive certain matrix moments that are used to illustrate the adaptivity of the different density models, and as a new domain for visual goodness-of-fit assessment. Sec. 4 presents experiments with airborne NASA/JPL AIRSAR data, and in Sec. 5 we give our conclusions.

2. STATISTICAL MODELLING

The full-polarimetric SAR instrument separately transmits orthogonally polarised microwaves pulses, and measures orthogonal components of the received signal. For each pixel, the measurements result in a matrix of scattering coefficients. These are complex-valued, dimensionless numbers that describe the transformation of the transmitted (incoming) electromagnetic (EM) field to the received (backscattered) EM field for all combinations of transmit and receive polarisation.

The transformation can be expressed as

$$\begin{bmatrix} E_h^r \\ E_v^r \end{bmatrix} = \frac{e^{jkr}}{r} \begin{bmatrix} S_{hh} & S_{hv} \\ S_{vh} & S_{vv} \end{bmatrix} \begin{bmatrix} E_h^t \\ E_v^t \end{bmatrix}, \quad (1)$$

where k denotes wavenumber and r is the distance between radar and target. The subscript of the EM field components E_i^j denotes horizontal (h) or vertical (v) polarisation, which is the most common set of orthogonal polarisations, while the superscript indicates transmitted (t) or received (r) wave. The scattering coefficients S_{ij} are subscripted with the associated receive and transmit polarisation, in that order. Together, they form the scattering matrix, denoted $\mathbf{S} = [S_{ij}]$.

The scattering matrix can be reduced to one of the vectors

$$\mathbf{s} = \begin{bmatrix} S_{hh} \\ (S_{hv}+S_{vh})/\sqrt{2} \\ S_{vv} \end{bmatrix} \text{ or } \mathbf{k} = \frac{1}{\sqrt{2}} \begin{bmatrix} S_{hh}+S_{vv} \\ S_{hh}-S_{vv} \\ S_{hv}+S_{vh} \end{bmatrix}. \quad (2)$$

The lexicographic scattering vector, denoted $\mathbf{s}$, is the vectorised version of $\mathbf{S}$ after the cross-polarisation terms S_{hv}

and S_{vh} have been averaged, assuming reciprocity of the target. The scaling with a factor $\sqrt{2}$ is done to preserve total power of the signal. The Pauli basis scattering vector, denoted $\mathbf{k}$, is a linear transformation of $\mathbf{s}$, which provides physical interpretations of its elements in terms of basic scattering mechanisms [5].

2.1. Gaussian Model

It is commonly assumed that the scattering vector elements are jointly circular complex Gaussian, even though this model only encompasses variability due to speckle, and not texture, which is discussed in the Sec. 2.2. The matrix $\mathbf{S}$ and the vectors $\mathbf{s}$ and $\mathbf{k}$ are single-look complex format representations of PolSAR data. The following derivations shall use $\mathbf{s}$ as the scattering vector, but would be equivalent for $\mathbf{k}$.

Multilook PolSAR data is commonly represented by

$$\mathbf{C} = \frac{1}{L}\sum_{i=1}^{L} \mathbf{s}_i \mathbf{s}_i^H \,, \tag{3}$$

known as the sample covariance matrix. It is formed as the mean Hermitian outer product of the single-look scattering vectors $\{\mathbf{s}_i\}_{i=1}^{L}$, where L is the nominal number of looks. The superscript H means complex conjugate transpose. Assume that $\mathbf{s}$ is zero mean and circular complex multivariate Gaussian, denoted $\mathbf{s} \sim \mathcal{N}_d^{\mathbb{C}}(\mathbf{0}, \boldsymbol{\Sigma})$, where $\mathbf{0}$ is a column vector of zeros, d is the dimension of $\mathbf{s}$, and $\boldsymbol{\Sigma} = \mathrm{E}\{\mathbf{s}\mathbf{s}^H\}$ is the covariance matrix of $\mathbf{s}$. The probability density function (pdf) of $\mathbf{s}$ is thus

$$p_{\mathbf{s}}(\mathbf{s}; \boldsymbol{\Sigma}) = \frac{1}{\pi^d |\boldsymbol{\Sigma}|} \exp(-\mathbf{s}^H \boldsymbol{\Sigma}^{-1} \mathbf{s}) \,, \tag{4}$$

where $|\cdot|$ is the determinant operator. It follows that if $L \geqslant d$ and the $\mathbf{s}_i$ in (3) are independent, then $\mathbf{C}$ follows the nonsingular complex Wishart distribution [6]:

$$\begin{aligned} &p_{\mathbf{W}}(\mathbf{C}; L, \boldsymbol{\Sigma}) \\ &\quad = \frac{L^{Ld} |\mathbf{C}|^{L-d}}{|\boldsymbol{\Sigma}|^L \Gamma_d(L)} \exp\left(-L \operatorname{tr}\left(\boldsymbol{\Sigma}^{-1}\mathbf{C}\right)\right) \,, \end{aligned} \tag{5}$$

where $\operatorname{tr}(\cdot)$ is the trace operator. The normalisation constant $\Gamma_d(L)$ is the multivariate Gamma function, defined as

$$\Gamma_d(L) = \pi^{d(d-1)/2} \prod_{i=0}^{d-1} \Gamma(L-i) \,, \tag{6}$$

where $\Gamma(L)$ is the standard Euler gamma function. In reality, the $\mathbf{s}_i$ are correlated, and this is compensated for by replacing L with an equivalent number of looks, $L_e \leqslant L$, in order to obtain consistency between moments of the theoretical model and sample moments of the data. This approximation provides a good model for the distribution of $\mathbf{C}$, denoted $\mathbf{C} \sim \mathcal{W}_d^{\mathbb{C}}(L_e, \boldsymbol{\Sigma})$.

2.2. Product Model

In addition to speckle, the randomness of a SAR measurement can also be attributed to texture. The notion of texture represents the natural spatial variation of the radar cross section, which is generally not perfectly homogeneous for pixels that are thematically mapped as one class. Several statistical models exist that incorporate texture, either by assuming statistics that imply a non-Gaussian scattering vector, or explicitly modelling texture as a separate random variable (rv). The latter case leads to a doubly stochastic model with a compounded distribution.

The well known product model, reviewed in [7, 8, 9], is shown to be both mathematically tractable and successful for modelling purposes. In the multilook polarimetric version [1], the polarimetric covariance matrix $\mathbf{C}$ is decomposed as a product of two independent stochastic processes with individual distributions:

$$\mathbf{C} = z\mathbf{W} \,. \tag{7}$$

One process, $\mathbf{W} \sim \mathcal{W}_d^{\mathbb{C}}(L_e, \boldsymbol{\Sigma})$, models speckle. The other process generates texture, represented by the scalar rv $z \in \mathbb{R}^+$, under the assumption that texture is independent of polarisation. The pdf of $\mathbf{C}$ depends on the distribution of z, which is normalised to unit mean.

Gamma Distributed Texture

The first covariance matrix distribution derived from the product model used the gamma distribution to model z [2]. A gamma distributed rv $z > 0$ has density

$$p_z(z; \alpha, \mu) = \left(\frac{\alpha}{\mu}\right)^{\alpha} \frac{z^{\alpha-1}}{\Gamma(\alpha)} \exp\left(-\frac{\alpha}{\mu} z\right) , \tag{8}$$

with shape parameter $\alpha > 0$ and mean value $\mu = \mathrm{E}\{z\} > 0$. This is denoted $z \sim \mathcal{G}(\alpha, \mu)$. The unitary mean texture rv is thus $z \sim \mathcal{G}(\alpha, 1)$. This leads to the matrix-variate $\mathcal{K}$ distribution for $\mathbf{C}$ [1, 2]:

$$\begin{aligned} &p_{\mathbf{C}}(\mathbf{C}; L_e, \boldsymbol{\Sigma}, \alpha) \\ &\quad = \frac{2|\mathbf{C}|^{L_e-d} (L_e\alpha)^{\frac{\alpha+L_e d}{2}}}{|\boldsymbol{\Sigma}|^{L_e} \Gamma_d(L_e) \Gamma(\alpha)} \left(\operatorname{tr}(\boldsymbol{\Sigma}^{-1}\mathbf{C})\right)^{\frac{\alpha-L_e d}{2}} \\ &\quad \times K_{\alpha-L_e d}\left(2\sqrt{L_e \alpha \operatorname{tr}(\boldsymbol{\Sigma}^{-1}\mathbf{C})}\right) . \end{aligned} \tag{9}$$

$K_n(\cdot)$ is the modified Bessel function of the second kind with order n. See [1, 10] for a detailed derivation.

Inverse Gamma Distributed Texture

The family of generalised inverse Gaussian distributions was proposed in [1] as a model for z. The gamma distribution is one special case. The inverse gamma distribution is another, which has been promoted in particular as

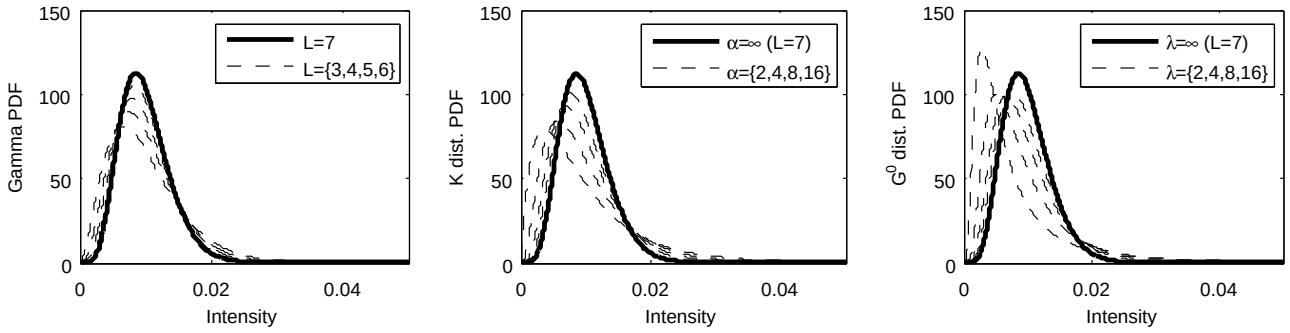

Figure 1. Examples of single intensity marginal densities for a polarimetric covariance matrix modelled by the relaxed Wishart distribution (left), matrix-variate $\mathcal{K}$ distribution (middle), and matrix-variate $\mathcal{G}^0$ distribution (right).

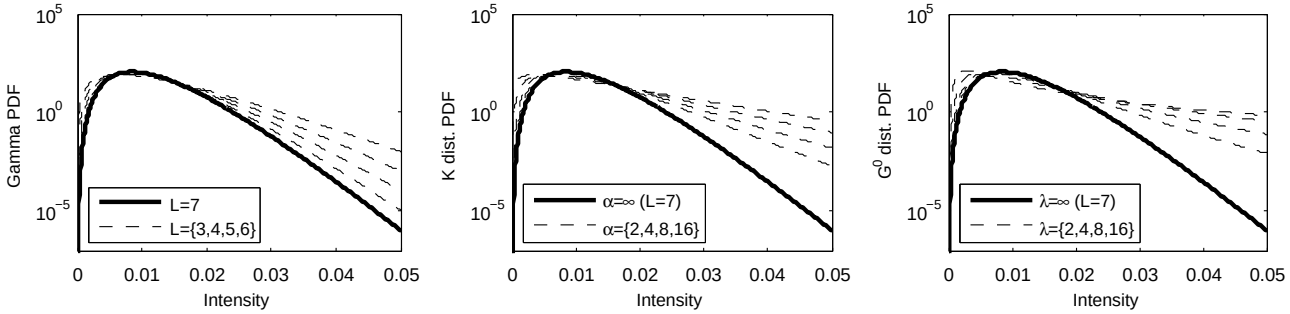

Figure 2. Same as Fig. 1 with logarithmic second axis to emphasize differences at the tails.

a good model for strongly heterogeneous clutter [1, 11]. Its pdf is given by

$$p_z(z;\lambda,\nu) = (\lambda\nu)^\lambda \frac{z^{-\lambda-1}}{\Gamma(\lambda)} \exp\left(-\frac{\lambda\nu}{z}\right) . \qquad (10)$$

This is denoted $z \sim \mathcal{G}^{-1}(\lambda,\nu)$, with shape parameter $\lambda > 0$ and $\nu > 0$. The normalised texture rv becomes $z \sim \mathcal{G}^{-1}(\lambda,(\lambda-1)/\lambda)$, which leads to the matrix-variate $\mathcal{G}^0$ distribution for $\mathbf{C}$ [1]:

$$\begin{aligned} &p_{\mathbf{C}}(\mathbf{C};L_e,\boldsymbol{\Sigma},\lambda) \\ &\quad = \frac{L_e^{L_e d}|\mathbf{C}|^{L_e-d}}{|\boldsymbol{\Sigma}|^{L_e}} \frac{\Gamma(L_e d+\lambda)(\lambda-1)^\lambda}{\Gamma_d(L_e)\Gamma(\lambda)} \\ &\quad \times \left(L_e \operatorname{tr}(\boldsymbol{\Sigma}^{-1}\mathbf{C}) + \lambda - 1\right)^{-\lambda-L_e d} . \end{aligned} \qquad (11)$$

For interpretation purposes, we note that $z \to 1$ and the distributions in Eqs. (9) and (11) converge in distribution to the complex Wishart distribution in Eq. (5) as $\alpha \to \infty$ and $\lambda \to \infty$, respectively. Thus, high values of α and λ imply little texture, whereas low values refer to significant texture and non-Gaussianity.

2.3. Relaxed Wishart Model

The standard Wishart model in Eq. (5) is parametrised by a constant L_e, which is estimated for the data set as a whole [3, 4]. We introduce a relaxed Wishart ($\mathcal{RW}$) model, whose functional form is identical. The difference is that L_e is replaced with a variable shape parameter, $\mathscr{L} \leqslant L_e$. Depending on the application, $\mathscr{L}$ is allowed to vary between classes (classification), segments (segmentation), or pixels (e.g., change detection). The new distribution is denoted by $\mathbf{C} \sim \mathcal{RW}_d^{\mathrm{C}}(\mathscr{L},\boldsymbol{\Sigma})$.

The motivation for this approach is explained by Fig. 1. It is not possible to visualise the effect of the distribution parameters directly on the pdfs in Eqs. (5), (9), and (11). We therefore plot their marginial densities for a single polarisation intensity. The respective marginals are gamma distributed, $\mathcal{K}_I$ distributed, and $\mathcal{G}_I^0$ distributed. For the latter two, the superscripted I denotes the multilook intensity version of the given distribution family.

In all the plots, the continuous curve represents the limiting case defined by the standard Wishart model, with a gamma distributed marginal pdf. In the left panel, the dashed curves show the evolution of the pdf under the $\mathcal{RW}$ model as $\mathscr{L}$ is lowered from the limit of $\mathscr{L} = L_e$. The same evolution is illustrated for the $\mathcal{K}$ distribution (middle panel) and the $\mathcal{G}^0$ distribution (right panel) for decreasing values of the respective texture parameters, α and λ. We observe that the effect of varying $\mathscr{L}$ resembles that induced by α and λ, even though a greater variation in shape is possible for the distributions based on the product model. Fig. 2 uses a logarithmic scale to highlight the heavy tails of the $\mathcal{K}$ and $\mathcal{G}^0$ distribution., which is less prominent for the marginal pdf of the $\mathcal{RW}$ distribution. We still conclude that $\mathscr{L}$ can be interpreted as a texture parameter alongside α and λ. Thus, the $\mathcal{RW}$ distribution implicitly models texture up to a moderate level.

3. GOODNESS-OF-FIT EVALUATION

This section discusses evaluation of the goodness-of-fit (GoF) for the matrix-variate density models of multilook PolSAR data. GoF testing in the literature has been limited to visual inspection of how well marginal densities of intensity fit histograms of the data. Classical statistical distribution tests, such as the Kolmogorov-Smirnov test or the Anderson-Darling test, are impractical in this case. As noted in [1], this is because they require binning of the domain of $\mathbf{C}$, which is the cone of positive definite matrices.

We here propose an alternative space where GoF evaluation can be performed. The idea is that GoF can be assessed by comparing theoretical moments of the models with sample moments computed from the data. We first define a new kind of matrix moments, that we call log-determinant cumulants. Closed form expressions for the candidate models are then derived. These are seen to have favourable properties that can be utilised to visualise the texture modelling capabilities of the models.

3.1. Log-determinant Cumulants

The following derivation is based on the application of second kind statistics, following the terminology introduced in [12]. Whereas the commonly known characteristic function is defined as the Fourier transform of a pdf, the second kind characteristic function is the Mellin transform of the pdf. This function can be used to generate moments and cumulants of the second kind, also termed log-moments and log-cumulants.

Let ξ be a real, positive rv with pdf $p_\xi(\xi)$. Start by defining the rth-order log-moment of ξ as

$$m_r(\xi) = \mathrm{E}\{(\ln \xi)^r\} = \left. \frac{d^r \phi_\xi(s)}{ds^r} \right|_{s=1} , \qquad (12)$$

where $\phi_\xi(s)$ is the Mellin transform of $p_\xi(\xi)$ and $s \in \mathbb{C}$ [12]. Then define the rth-order log-cumulant of ξ as

$$\kappa_r(\xi) = \left. \frac{d^r \psi_\xi(s)}{ds^r} \right|_{s=1} , \qquad (13)$$

where $\psi_\xi(s) = \ln \phi_\xi(s)$. Relations between some low-order log-moments and log-cumulants are given by

$$\kappa_1 = m_1 , \qquad (14)$$
$$\kappa_2 = m_2 - m_1^2 , \qquad (15)$$
$$\kappa_3 = m_3 - 3m_1 m_2 + 2m_1^3 . \qquad (16)$$

It follows from a fundamental property of the Mellin transform [12] that for a product of independent random variables, $\xi = \rho \cdot \zeta$, with $\rho, \zeta > 0$:

$$\kappa_r(\xi) = \kappa_r(\rho) + \kappa_r(\zeta) , \quad \forall r \in \mathbb{N} . \qquad (17)$$

This equips us to derive the log-cumulant of $|\mathbf{C}|$, which will be referred to as the log-determinant cumulant (LDC) of $\mathbf{C}$.

Note that $|\mathbf{C}| = |z\mathbf{W}| = z^d |\mathbf{W}|$. Thus,

$$\kappa_r(|\mathbf{C}|) = d^r \kappa_r(z) + \kappa_r(|\mathbf{W}|) . \qquad (18)$$

The log-cumulants of z have been derived in [12]. For $z \sim \mathcal{G}(\alpha, \mu)$ it was shown that

$$\kappa_1(z) = \ln\left(\frac{\mu}{\alpha}\right) + \Psi^{(0)}(\alpha) , \qquad (19)$$
$$\kappa_r(z) = \Psi^{(r-1)}(\alpha) , \quad r > 1 , \qquad (20)$$

where $\Psi^{(r)}(z)$ is Euler's polygamma function of order r. The log-cumulants of $z \sim \mathcal{G}^{-1}(\lambda, \nu)$ were found as

$$\kappa_1(z) = \ln \lambda\nu - \Psi^{(0)}(\lambda) , \qquad (21)$$
$$\kappa_r(z) = (-1)^r \, \Psi^{(r-1)}(\lambda) . \qquad (22)$$

The LDCs of the Wishart distributed $\mathbf{W}$ can be deduced from results found in [3, 4] as

$$\kappa_1(|\mathbf{W}|) = \ln|\mathbf{\Sigma}| + \sum_{i=0}^{d-1} \Psi^{(0)}(L_e - i) - d \ln L_e \qquad (23)$$

$$\kappa_r(|\mathbf{W}|) = \sum_{i=0}^{d-1} \Psi^{(r-1)}(L_e - i) , \quad r > 1 . \qquad (24)$$

This completes the expression in Eq. (18) for our candidate models.

3.2. Log-determinant Cumulant Diagram

Note that the LDCs are matrix-variate generalisation of the log-cumulants derived in [12] for the single polarisation product model. As in the one-dimensional case, we can utilise the fact the LDCs do not depend on the scale parameter $\mathbf{\Sigma}$ for $r > 1$. More specifically, the $\kappa_{r>1}(|\mathbf{C}|)$ depend only on the texture parameters:

$$\kappa^{\mathcal{W}}_{r>1}(|\mathbf{C}|) = \sum_{i=0}^{d-1} \Psi^{(r-1)}(L_e - i) \qquad (25)$$

$$\kappa^{\mathcal{K}}_{r>1}(|\mathbf{C}|) = d^r \Psi^{(r-1)}(\alpha) + \sum_{i=0}^{d-1} \Psi^{(r-1)}(L_e - i) \qquad (26)$$

$$\kappa^{\mathcal{G}^0}_{r>1}(|\mathbf{C}|) = (-d)^r \Psi^{(r-1)}(\lambda) + \sum_{i=0}^{d-1} \Psi^{(r-1)}(L_e - i) \qquad (27)$$

$$\kappa^{\mathcal{RW}}_{r>1}(|\mathbf{C}|) = \sum_{i=0}^{d-1} \Psi^{(r-1)}(\mathscr{L} - i) , \qquad (28)$$

where the superscript of κ indicates which model the expression describes.

By plotting two LDCs of different orders against each other, we obtain a curve in LDC space which depicts the

paired LDC values that can be attained under a given model. We refer to this as an LDC diagram. Sample LDCs calculated from data can be overlaid the model curves, and the diagram used to assess how well the data are described by different models, and which model provides the best fit. Diagrams of second and third order log-cumulants were plotted in [12, 13], and we will use the same orders for our LDC diagrams. Remark that the bias and variance of the sample LDCs are expected to increase rapidly with order.

4. EXPERIMENTS

4.1. Marginal Densities of Intensity

We have extracted three test samples from an L-band quadrature polarisation image aquired by the airborne NASA/JPL AIRSAR sensor over Flevoland, the Netherlands, in August 1989. The samples are taken from some of the more textured areas in the image. One is from a forest area and the other two from different crops. Marginal densities of the intensity in the HH, HV, and VV channels for the forest sample are shown in Fig. 3. These densities describe unfiltered data. Fig. 4 describes the same data after they have been filtered with a refined Lee filter [14] of window size 7×7.

The first observation is that the data are well described by all the models in Fig. 3. By zooming in on the densities, it may be concluded by visual inspection that the $\mathcal{K}$ model provides the best fit, followed by the $\mathcal{RW}$ model. The ENL estimated for the data set, and used to parametrise the standard Wishart, $\mathcal{K}$, and $\mathcal{G}^0$ model, is $L_e = 3.3$. This constant is replaced with $\mathscr{L} = 2.53$ for the $\mathcal{RW}$ model. The texture parameters α and λ are estimated with the method described for the $\mathcal{K}$ distribution in [10].

Fig. 4 shows that the models have very different GoF for speckle filtered data. The Wishart model is the worst fit, and none of the distributions based on the product model produce an adequate result either. Only the $\mathcal{KW}$ model seems to do a good job. The ENL was estimated to $L_e = 48$, and is reduced to $\mathscr{L} = 27$ for the $\mathcal{RW}$ model. The marginal densities of the other two test samples yield very similar results, both before and after speckle filtering, and are therefore not shown.

4.2. Log-determinant Cumulant Diagrams

Fig. 5 shows a LDC diagram where $\kappa_3(|\mathbf{C}|)$ is plotted against $\kappa_2(|\mathbf{C}|)$, with analogy to the log-cumulant diagrams in [12, 13]. The Wishart model has no texture parameter, and its LDCs are therefore constant, equal to the contribution $\kappa_r(|\mathbf{W}|)$, $r = 1, 2$ of the Wishart distributed speckle matrix. These constants are indicated in the figure by the dotted lines, intersecting at the point which describes the Wishart model. The possible LDC pairs of the $\mathcal{K}$, $\mathcal{G}^0$, and $\mathcal{RW}$ models lie on a curve parametrised by α, λ, and $\mathscr{L}$, respectively. The asymptotic behaviour of these curves, as the texture parameters decrease towards their lower limits, is indicated on the figure. At the upper limit, the curves all converge to the Wishart case. Sample LDCs of the three test samples are plotted as points in green (forest), cyan, and magenta (two different crops). We plot a collection of sample LDC estimates, obtained by bootstrap sampling of the full test samples, in order to illustrate the dispersion of the sample estimates. ENL estimates for each test sample are shown in the figure.

Diagrams of data before and after speckle filtering are presented in the left and right panel, respectively. For the unfiltered data, the LDC diagram clearly indicates that the $\mathcal{RW}$ distribution is the best model for the forest sample. The other test samples are less textured, and all models are adequate. For the speckle filtered data, the LDC diagram suggests that the $\mathcal{RW}$ model fits best for the forest sample and the first crop sample (cyan), while the $\mathcal{K}$ model performs best for the second crop sample (magenta). For the crop samples, both the $\mathcal{RW}$ model and the $\mathcal{K}$ model fit reasonably well. The Wishart and the $\mathcal{G}^0$ model are inadequate in all cases. The LDC diagram indicates good fit of the $\mathcal{K}$ model to the crop samples, which is not compatible with observations of the marginal densities (not shown). This prompts us to reconsider the estimator for α (and λ) in future work.

The success of the $\mathcal{RW}$ distribution in modelling of speckle filtered data, and the relative failure of the others, can be explained by a discussion of the nature of adaptive speckle filters. Adaptive speckle filters apply variable smoothing by consideration of local homogeneity. Hence, the ENL is mapped from a constant value to a dispersed range of values. This is not modelled appropriately, neither by the Wishart distribution nor the other distributions based on the product model. The $\mathcal{RW}$ distribution, on the other hand, apparently represents a better approach.

5. CONCLUSIONS

We have proposed a relaxed Wishart distribution where the equivalent number of looks of the standard Wishart model has been replaced by a varable shape parameter. We have further derived the log-determinant cumulants of the polarimetric covariance (or coherency) matrix under the product model, and demonstrated how they can be utilised in visual inspection of goodness-of-fit for matrix-variate distributions. Experimental results show that for a moderate level of texture, the newly proposed density can compete with densities derived from the product model with regards to modelling of unfiltered PolSAR data. For data that are processed with an adaptive speckle filter, the relaxed Wishart model is shown to perform better. Based on the very promising results, we suggest that the relaxed Wishart distribution should be tested more extensively on other data sets and with different speckle filters. It should also be applied to model-based classification, change detection, and other image analysis tasks.

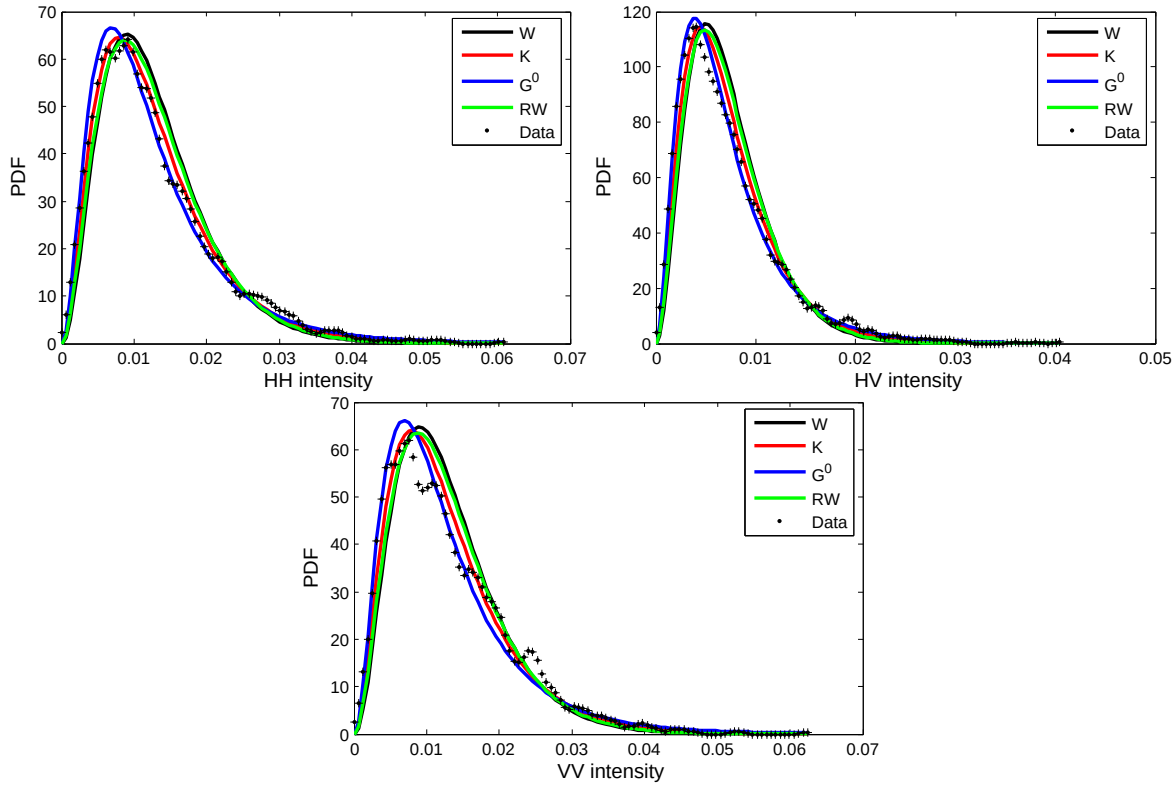

Figure 3. Comparison of marginal densities of the Wishart, $\mathcal{RW}$, $\mathcal{K}$, and $\mathcal{G}^0$ distribution with data histograms for a textured forest area in the AIRSAR L-band image of Flevoland. No speckle filter applied.

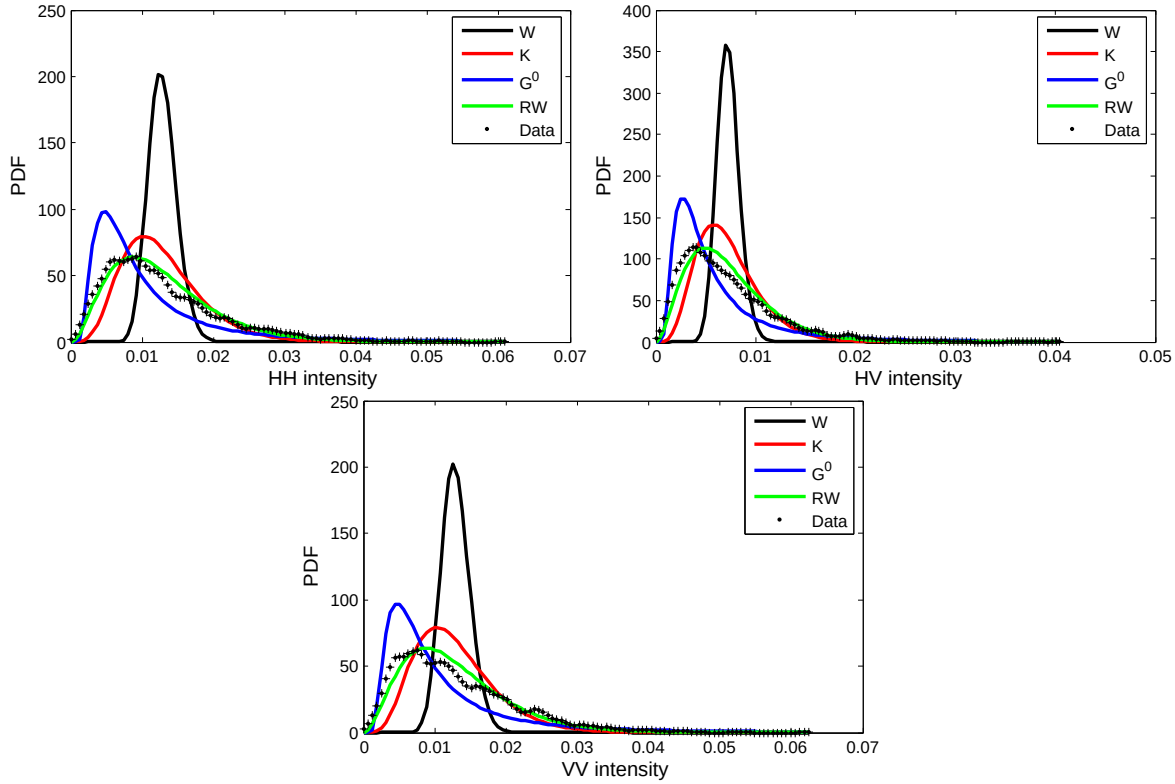

Figure 4. Comparison of marginal densities of the Wishart, $\mathcal{RW}$, $\mathcal{K}$, and $\mathcal{G}^0$ distribution with data histograms for a textured forest area in the AIRSAR L-band image of Flevoland. Modified Lee filter with window size 7×7 applied.

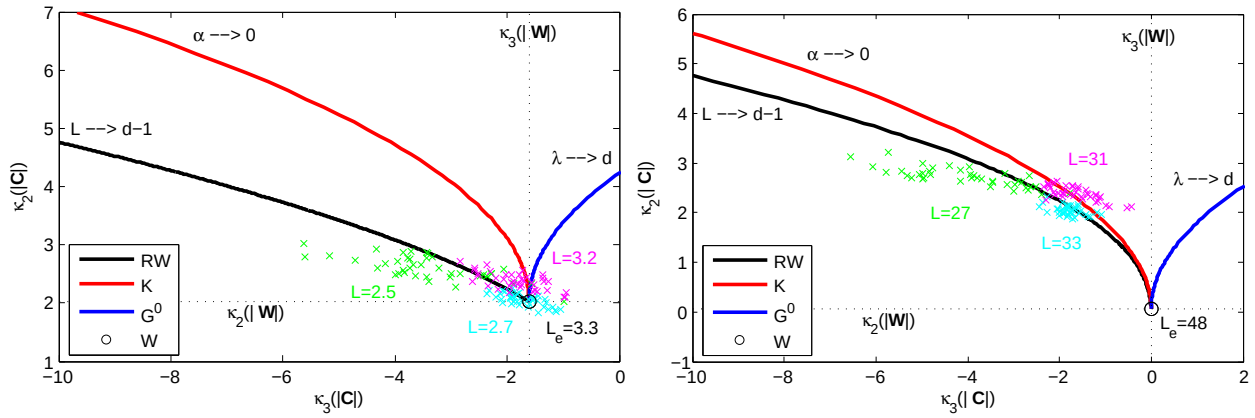

Figure 5. Diagram of second and third-order log-determinant cumulants (LDCs) for the Wishart, $\mathcal{RW}$, $\mathcal{K}$, and $\mathcal{G}^0$ distribution. Sample LDCs for three test samples from the AIRSAR L-band image of Flevoland are plotted in green (forest), cyan and magenta (two different crops). Results are shown before (left panel) and after (right panel) speckle filtering with a 7×7 refined Lee filter.

ACKNOWLEDGEMENTS

The authors would like to thank NASA/JPL-Caltech for making available the AIRSAR data set used in the paper. We further thank the European Space Agency and the POLSARPRO software development team for their continued efforts in publishing open source software and PolSAR data samples.

REFERENCES

1. C. C. Freitas, A. C. Frery, and A. H. Correia, "The polarimetric $\mathcal{G}$ distribution for SAR data analysis," *Environmetrics*, vol. 16, no. 1, pp. 13–31, Feb. 2005.

2. J.-S. Lee, D. L. Schuler, R. H. Lang, and K. J. Ranson, "K-distribution for multi-look processed polarimetric SAR imagery," in *Proc. IEEE Int. Geosc. Remote Sensing Symp., IGARSS'94*, vol. 4, Pasadena, USA, Aug. 1994, pp. 2179–2181.

3. S. N. Anfinsen, A. P. Doulgeris, and T. Eltoft, "Estimation of the equivalent number of looks in PolSAR imagery," in *Proc. IEEE Int. Geosc. Remote Sensing Symp., IGARSS'08*, vol. 4, Boston, USA, July 2008, pp. 487–490.

4. ——, "Estimation of the equivalent number of looks in polarimetric synthetic aperture radar imagery," *IEEE Trans. Geosci. Remote Sensing*, in review.

5. J.-S. Lee, M. R. Grunes, T. L. Ainsworth, D. L. Schuler, and S. R. Cloude, "Unsupervised classification using polarimetric decomposition and the complex Wishart distribution," *IEEE Trans. Geosci. Remote Sensing*, vol. 37, no. 5, pp. 2249–2259, Sept. 1999.

6. N. Goodman, "Statistical analysis based on a certain multivariate complex Gaussian distribution (an introduction)," *Ann. Math. Statist.*, vol. 34, no. 1, pp. 152–177, Mar. 1963.

7. C. Oliver and S. Quegan, *Understanding Synthetic Aperture Radar Images*, 2nd ed. SciTech Publishing, 2004.

8. R. Touzi, W. M. Boerner, J.-S. Lee, and E. Lüneburg, "A review of polarimetry in the context of synthetic aperture radar: Concepts and information extraction," *Can. J. Remote Sensing*, vol. 30, no. 3, pp. 380–407, 2004.

9. S. H. Yueh, J. A. Kong, J. K. Jao, R. T. Shin, and L. M. Novak, "K-distribution and polarimetric terrain radar clutter," *J. Electrom. Waves Applic.*, vol. 3, no. 8, pp. 747–768, 1989.

10. A. P. Doulgeris, S. N. Anfinsen, and T. Eltoft, "Classification with a non-Gaussian model for PolSAR data," *IEEE Trans. Geosci. Remote Sensing*, vol. 46, no. 10, pp. 2999–3009, Oct. 2008.

11. A. C. Frery, H.-J. Müller, C. C. F. Yanasse, and S. J. S. Sant' Anna, "A model for extremely heterogeneous clutter," *IEEE Trans. Geosci. Remote Sensing*, vol. 35, no. 3, pp. 648–659, May 1997.

12. J.-M. Nicolas, "Introduction aux statistique de deuxième espèce: Application des logs-moments et des logs-cumulants à l'analyse des lois d'images radar," *Traitement du Signal*, vol. 19, no. 3, pp. 139–167, 2002, in French.

13. ——, "A Fisher-MAP filter for SAR image processing," in *Proc. IEEE Int. Geosc. Remote Sensing Symp., IGARSS'03*, vol. 3, Toulouse, France, July 2003, pp. 1996–1998.

14. J.-S. Lee, M. R. Grunes, and G. de Grandi, "Polarimetric SAR speckle filtering and its implication for classification," *IEEE Trans. Geosci. Remote Sensing*, vol. 37, no. 5, pp. 2363–2373, Sept. 1999.